Unveiling the Inner Structure of Micrometric Hollow Polymeric Fibers Using Synchrotron X-ray Nanotomography

Jorge Torre[1,2,3*], P. Cimavilla-Roman[1], D. Cuadra-Rodriguez[1,3], M. A. Rodriguez-Perez[1,2], Peter Guttmann[4], Stephan Werner[4], Javier Pinto[1,2,3], Suset Barroso-Solares[1,2,3*],

[1]*Cellular Materials Laboratory (CellMat), Condensed Matter Physics, Crystallography, and Mineralogy Department, Faculty of Science, University of Valladolid (Spain)*

[2]*BioEcoUVA Research Institute on Bioeconomy, University of Valladolid (Spain)*

[3]*Study, Preservation, and Recovery of Archaeological, Historical and Environmental Heritage (AHMAT) Research Group, Condensed Matter Physics, Crystallography, and Mineralogy Department, Faculty of Science, University of Valladolid (Spain)*

[4] *Helmholtz-Zentrum Berlin für Materialien und Energie, Dep. X-Ray Microscopy, Electron Storage Ring at BESSY II, Berlin, (Germany)*

[*]Corresponding author: Jorge Torre (jorge.torre@uva.es) +34 662 072 871, Suset Barroso-Solares (suset.barroso@uva.es)

ABSTRACT

In this study, a novel application of synchrotron X-ray nanotomography based on high-resolution full-field transmission X-ray microscopy (TXM) for characterizing the structure and morphology of micrometric hollow polymeric fibers is presented. By employing post-image analysis using an open-source software such as Tomviz and ImageJ, various key parameters in fibers morphology, including diameter, wall thickness,

wall thickness distribution, pore size, porosity, and surface roughness were assessed. Electrospun polycaprolactone (PCL) fibers with micrometric diameters and submicrometric features with induced porosity via gas dissolution foaming were used to this aim. The acquired synchrotron X-ray nanotomography data was analyzed using two approaches: 3D tomographic reconstruction and 2D radiographic projections-based analysis. The results of the combination of both approaches demonstrate unique capabilities of this technique, not achievable by other available techniques, allowing for a full characterization of the internal and external morphology and structure of the fibers as well as to obtain valuable qualitative insights into the overall fiber structure.

Keywords: *Characterization, polycaprolactone, morphology, image analysis, 3D reconstruction, wall thickness, pore size, surface roughness.*

1. INTRODUCTION

Electrospun polymeric fibers have recently become particularly appealing in a wide variety of fields, such as bioengineering, biotechnology, energy, electronics, defense, and security, etc. (Salem, 2001; Barhoum, 2019). The versatility of electrospinning allows not only to produce fibers with exceptional properties, such as high area-to-volume ratio, high porosity or high mechanical flexibility, among others, but also to produce tailored fibers adapted to every specific applications (Ariff et al., 2016; Stanger et al., 2005). In particular, electrospun fibers have shown great potential in biomedical applications, such as drug delivery (Duan et al., 2022; Williams et al., 2018), tissue engineering (Lucy A Bosworth, 2011), or wound healing (Xinkuan Liu et al., 2021), due to their ability to mimic the native extracellular matrix of tissues and organs. Other applications outside the

biomedicine field include water treatment (Barroso-Solares et al., 2016), sensors (Halicka & Cabaj, 2021), filters (Valencia-Osorio & Álvarez-Láinez, 2021), etc.

The morphology and structure of the fibers are crucial in determining their performance and suitability for each specific application (Li & Wan, 2017; Bhat, 2017). Some of the most commonly used parameters to describe the morphology of electrospun fibers include the average fiber diameter and distribution, pore size and porosity, surface area, and surface roughness (Barhoum, 2019; Ramakrishna et al., 2005). For example, reducing the fiber diameter can enhance mechanical strength and stiffness (Wong et al., 2008), and inducing porosity can lead to higher specific areas, making the fiber mat a promising candidate for tissue engineering or filtration membranes (Soliman et al., 2011). Additionally, increasing fibers surface roughness also contributes to maximizing the available surface area without merely relying on decreasing the fiber diameter, which renders them highly appropriate for some biomedical applications (Laijun Liu et al., 2021; Ferreira et al., 2015).

Besides that, hollow fibers have gained significant attention in recent years, as their structure provides an additional way of achieving larger surface-to-volume ratio compared to solid fibers (Vohra et al., 2023). Albeit the fabrication of hollow fibers can be challenging, recent advancements have paved the way for more precise and efficient manufacturing methods (Vohra et al., 2023; Tian et al., 2021). Among the various available techniques, a few have proved to be reliable in hollow fiber fabrication (Tian et al., 2021). For example, co-axial electrospinning involves the simultaneous electrospinning of two polymer solutions in a co-axial spinneret, where one solution forms the shell and the other the core of the hollow fiber. After the solidification, the core

can be removed mixing it with a solvent immiscible in the shell, obtaining the hollow fiber (Han & Steckl, 2019; Elahi & Lu, 2013). In co-extrusion, similarly, a spinneret with two concentric orifices is used as well. The outer orifice delivers the shell, while the inner orifice carries a core polymer solution that serves as a removable template (Tian et al., 2021). However, in this case, the solutions are extruded from the tubes and are rapidly passed through a coagulation bath, in which the outer layer is solidified using a cross-linking reaction. After the removal of the core layer, the hollow fiber is obtained. Both of these techniques need to have precise control of a wide variety of parameters, not only in the process itself, but also in the polymeric solution (DeFrates et al., 2018). In order to produce hollow fibers with diameter down to a few microns in a simpler way which does not require such strict control of the experiment conditions, an additional very recent technique proposed by Barroso-Solares *et al.* (Barroso-Solares et al., 2020) has proved reliable. It works by producing solid fibers following a conventional electrospinning approach and subsequently saturating the fiber mat with CO_2 at high pressure causing the formation of axial holes inside and pores on the fibers surface by releasing the pressure (gas dissolution foaming (GDF)). GDF is a well-known environmentally friendly technique to produce porous polymers (Kumar & Suh, 1988; Cuadra-Rodríguez et al., 2022; Ventura et al., 2018). However, the use of GDF on polymer samples with dimensions in the micrometric range or below have been elusive until the recent development of a novel approach using gas diffusion barriers (Barroso-Solares et al., 2020; Cuadra-Rodríguez et al., 2022; Orsi et al., 2014). In the case of polymeric fibers, this approach has proved to be able to tune the surface porosity, as well as to provide a hollow structure by merging of the inner pores (Barroso-Solares et al., 2020). Hollow fibers produced with this method can reach diameters of only a few units of micrometers, showing features such as wall thickness or pores within hundreds of nanometers, which

hinders the accurate characterization of their morphology by using conventional techniques.

Accurate and comprehensive methods for characterizing fibers morphology and structure are essential for optimizing fabrication processes and further developing their applications. In recent years, there has been a growing interest in developing new methods for this purpose (Barhoum, 2019; Mitchell, 2011; Singh & Singh, 2021). While conventional techniques, such as scanning electron microscopy (SEM) (Doan et al., 2016; Angel et al., 2020) transmission electron microscopy (TEM) (Yoshioka et al., 2010; He et al., 2006), and atomic force microscopy (AFM) (Casper et al., 2004; Ji et al., 2006) have been widely used to analyze the morphology of electrospun fibers, these techniques are often limited in their ability to provide detailed information on the internal structure of fibers (Sensini et al., 2018). For instance, assessing parameters like wall thickness distribution in hollow fibers or the continuity of hole within them is challenging using the aforementioned techniques. Moreover, the resolution of X-ray-tomography-based techniques at laboratory scales often falls short when attempting to investigate features of fibers with sizes close to the nanoscale. In such cases, synchrotron X-ray tomography emerges as a highly valuable technique. Its use enables exceptional spatial resolution, facilitating the visualization and analysis of a wide range of materials with unprecedented detail (Shen et al., 2004; Wang et al., 2017; Das et al., 2022; Lang et al., 2023). In particular, high-resolution full-field TXM synchrotron X-ray nanotomography proves very useful in situations where μCT techniques struggle to provide the necessary resolution and comprehensive analysis of internal structures.

The high-resolution TXM X-ray nanotomography field is currently an area of active research and innovation. In the context of porous materials characterization, the technique has emerged as a versatile tool, allowing for the detailed analysis of internal structures and dimensions in various materials (Wang et al., 2016; Xiaoyang Liu et al., 2021; Zou et al., 2020; Chen et al., 2023).

In the case of polymeric fibers, a limited number of researchers have already approached structural characterization using any kind of synchrotron X-ray tomography. Recently, authors such as Sensini *et al.* (Sensini et al., 2018), Svetlana Shkarina *et al.* (Shkarina et al., 2018), and Jekaterina Maksimcuka *et al.* (Maksimcuka et al., 2017), assessed macroscopic electrospun fiber orientation in bundles and scaffolds with this technique, which proved synchrotron X-Ray Computed Nanotomography reliable for this purpose, when complemented with SEM analysis. Another notable example is the work carried out by Jens Vinge Nygaard *et al.* (Nygaard et al., 2011), which demonstrated the capabilities of the technique to study details of the internal morphology of single fibers or beads with diameters in the nanometers range.

Despite the aforementioned advantages of synchrotron X-ray nanotomography, it is important to acknowledge certain limitations associated with the technique. One notable limitation is that an increase in spatial resolution typically comes at the expense of a reduced field of view. In the TXM setup utilized for this work the FOV was restricted to 26.0 μm at a pixel size of $20\,nm$. This means that in a single synchrotron X-ray nanotomography analysis, it became impractical to analyze more than a segment of typically less than fifty micrometers (Blykers et al., 2021; Cimavilla-Román et al., 2022). Also, it is important to consider the potential for sample damage during the preparation

process. Manipulating and handling the delicate fibers during sample preparation can lead to deformations or alterations in the fiber morphology, which can impact the accuracy and reliability of the obtained results. Furthermore, it is worth noting some high-resolution full-field TXM synchrotron setups for X-ray nanotomography, as in this case, might be constrained in their ability to achieve nanometric resolution data. To overcome this limitation, specific experimental setups are required to enhance the resolution capabilities. However, due to technical considerations, high-resolution TXM X-ray nanotomography at synchrotron facilities are sometimes restricted to the use of tilt tomography over rotational tomography. Tilt tomography involves acquiring images at a limited range of angles instead of full rotational scans, which pose challenges in the reconstruction process (Barutcu et al., 2021). In this case, the missing range of angles is comparable to EM tomography, however, the tilt range was large enough to minimize its effects, as proved by the results below.

Herein, the accuracy of the synchrotron X-ray nanotomography technique for the structural and morphological characterization of individual pure and hollow polymeric microfibers will be examined, considering the inherent limitations associated with this method. For this, a comprehensive analysis will be conducted using two approaches: one involving the utilization of 3D reconstruction from tomographic data, and other relying solely on the analysis of radiographic 2D images. By comparing the results obtained from both approaches, the reliability and consistency of the data obtained from the 3D reconstruction will also be assessed. It is important to clarify that the study will be focused on the characterization of individual fibers rather than the properties of the entire fiber mat.

2. MATERIALS AND METHODS

2.1 Materials

The materials employed included Polycaprolactone (PCL) ($M_n = 80.000, \rho = 1.15 \frac{g}{cm^3}$, melting temperature $T_m = 61\,°C$), purchased from Sigma-Aldrich (USA) and Poly (vinyl alcohol) (PVOH) (Mowiflex C17, $\rho = 1.25\, g/cm^3$, glass transition temperature (T_g) $= 60\,°C$ and $T_m = 170\,°C$) that was gently provided by Kuraray. Chloroform was sourced from Scharlab (Barcelona, Spain). Deionized water and medical-grade carbon dioxide (CO_2) with a purity of 99.9% were utilized in the incorporation and removal of the gas diffusion barriers and foaming processes, respectively.

2.2 Fibers preparation

The fibers studied in this work were produced using the procedure detailed in a previous work (Barroso-Solares et al., 2020). In brief, the fabrication of solid fibers involved electrospinning a $10\ wt.\%$ PCL solution in chloroform at a voltage of $15\ kV$, flow rate of $1\ mL \cdot h^{-1}$, and collector distance of $20\ cm$, resulting in fiber mats with controlled thicknesses of around 200 μm. Then, the solid fibers were subjected to a gas dissolution foaming (GDF) procedure after being imbibed within a $300\ \mu m$ thickness film of PVOH obtained from a $5\ wt.\%$ solution in water. The GDF was performed with CO_2 during 24 hours at 30 MPa and 45 ºC. Then, the PVOH coating was completely removed from the foamed fibers by immersing them into a 60ºC water bath before their characterization.

2.3 Scanning Electron Microscopy (SEM)

Scanning electron microscopy (SEM) was first employed to characterize the fibers coating the surface with gold. It served as a reference for the subsequent analysis. SEM allowed for the detailed visualization of fiber surface morphology and homogeneity which helped demonstrate structural integrity and overall quality of the fibers. The device model was FlexSEM 1000, Hitachi.

2.4 Synchrotron X-ray Nanotomography

High resolution X-ray synchrotron nanotomography experiments were performed at the XM – X-ray Microscopy beamline (Guttmann et al., 2018; Werner et al., 2023), a beamline at BESSY II facility of the Helmholtz-Zentrum Berlin in Berlin (Germany). The X-ray microscope was equipped with Fresnel zone plate objective with an outermost zone width of 25 nm resulting in a 3D resolution of about 36 nm (Schneider et al., 2012). The X-ray detector was a thinned, backside illuminated CCD, $1340x1300$ pixels (Roper Scientific PI SX1300). The photon energy of the X-rays used for the experiment was fixed to 1.0 keV. The selected exposure time of the detector was around 3 to 4 s, the tilt step was 1º and the number of projections varied between samples but always being greater than 70. The acquisition time for a full tomographic data set was about $20 - 30$ min, the field of view was set to 26.0 µm and the reconstructed images achieved a pixel size of 20.0 nm.

Individual fibers were manually separated with tweezers from the produced fiber mats and located into the sample holder for the X-ray nanotomography experiments. Each fiber was studied at different positions along their length, aiming to overcome the limitations of the narrow field of view. Two individual reference solid fibers were studied

by performing seven X-ray tomographs, while up to four individual hollow fibers, obtained from different foamed fiber mats, were studied by performing fifteen tomographs. This raw data went through preliminary screening, discarding the tomographs in which the fibers could not be properly aligned, exceeded the field of view, their visualization was obstructed by other elements, or present particular morphologies that makes data interpretation difficult (see **Supplementary Information, Section 1**). From this screening, nine data sets were selected for this work (see **Table 1**). In particular, one solid fiber (F1) was studied as a reference homogeneous material, as well as three hollow fibers (F2, F3, and F4). It should be noted that the selected solid fiber is not representative of the average diameter of the fiber mats (i.e., about 5-8 μm) (Barroso-Solares et al., 2020), but it was selected for this study due to the high contrast provided for the study of surface features. Moreover, it should be taken into account that the quantitative values provided by this work are limited to a very small number of individual fibers, which could be, as in the case of the solid fiber, non-presentative of the average features of the fiber mats from which they were extracted. Therefore, these values should be understood as a proof of concept of the proposed characterization approach and its capabilities, and not as representative overall features of the studied materials.

Table 1. Fibers used in the study.

Fiber name	Samples	Fabrication method	External Diameter (μm)
F1	1, 2, 3	Solid fiber	16.9 ± 0.4
F2	4, 5	GDF at 45º C, 30 MPa	12.3 ± 1.2
F3	6	GDF at 45º C, 30 MPa	9.4 ± 1.6
F4	7, 8, 9	GDF at 45º C, 30 MPa	8.8 ± 1.4

2.5 Tomography data preprocessing

The data obtained from synchrotron X-ray nanotomography was subsequently processed using two distinct approaches, each allowing for the characterization of different fiber parameters. This was carried out with the aim of covering the gaps that

could not be addressed with each method separately and evaluating the reliability and completeness of this approach for fiber characterization.

The first approach involved performing a 3D reconstruction using the software Tomviz (Anon, n.d.), which permits the visualization and manipulation of the volumetric dataset. The reconstructed 3D image provided a comprehensive view of the internal structure and morphology of the electrospun fibers. This enabled the extraction of qualitative information regarding parameters such as shape, diameter, and wall thickness. The 3D reconstruction data was further analyzed using ImageJ (Abràmoff et al., 2004), a powerful image analysis software, to extract specific measurements and perform quantitative analyses on the reconstructed 3D image.

A second approach involved the direct analysis of the radiography images obtained during synchrotron X-ray nanotomography without performing the 3D reconstruction step. These images, representing 2D projections of the sample at various angles, were also analyzed using ImageJ. This allowed for the extraction of quantitative information directly from the 2D images. Parameters such as fiber diameter, wall thickness, surface roughness, pore size and porosity could be evaluated with this technique. Moreover, while 2D projections can provide some insight into the continuity of the hollow structure, the use of 3D reconstructions allows for a more detailed and explicit demonstration of this continuity and openness along the entire length of the fiber segments. By employing 3D reconstructions in addition to the 2D projections, a more comprehensive and precise confirmation of the observed continuity can be obtained, also ensuring the reliability and accuracy of the results obtained from the 2D projections.

2.6 Determination of the fiber parameters

Fiber diameter

In order to determine the fiber diameter, a straightforward approach was adopted using the 2D projections. Diametral lines were manually drawn along the length of the fiber, considering various projections to capture its three-dimensional nature (see **Supplementary Information, Section 1.1**). This enabled a more accurate assessment of the fiber diameter from different viewing angles. The value of the fiber diameter was the average of the different diameters taken.

Wall thickness

Fibers wall thickness (t) was determined using both the 2D projections and the 3D reconstructions importing the data to ImageJ. Using the "Plot profile" tool made possible to quantify the fiber wall thickness by measuring the distance between the maximum and minimum value of the intensity profile peak along specific regions of interest (ROIs) within the stack of images (see **Figure 1**). In order to do this for every slice of the stack, a custom script was utilized (Torre, 2023). Both walls at both sides were analyzed, leading to the pair of thickness values t_1 and t_2. However, given that each slice in the 2D projections stack corresponds to a different tilt angle, so would each measured thickness. Therefore, all values were averaged at the end. A more detailed explanation can be found in the **Supplementary Information, Section 1.2**.

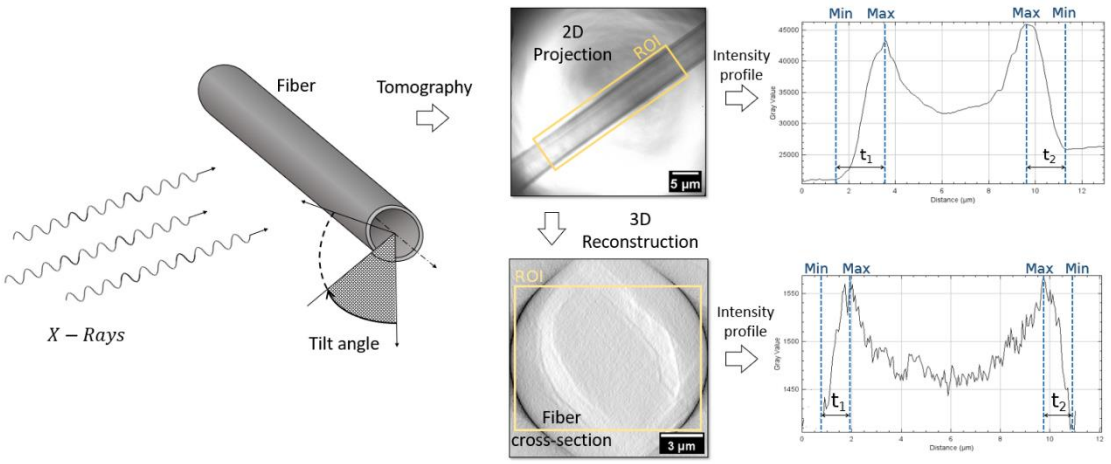

Figure 1. Schematic visualization of the wall thickness calculation using both 2D projections and fiber cross-section from the 3D reconstruction.

Wall thickness distribution

In order to assess the wall thickness distribution along the fiber length, a similar approach to the previous parameter was employed using the 2D projections. A custom script was developed to define a moving region of interest (ROI) along the length of the fiber, allowing for the calculation of the wall thickness at different positions (Torre, 2023). This method enabled the examination of the variation in wall thickness along the fiber, providing insights into the uniformity or heterogeneity of the fiber structure and morphology. By analyzing the variations in wall thickness along the fiber length, it was possible to identify regions where the wall thickness remained almost constant, indicating the possibility of a continuous hollow structure.

Pore size

Similar to the methodology commonly employed for images derived from scanning electron microscopy (SEM), the pore size can be determined using ImageJ by manually contouring each visible cell or pore within the images obtained from the X-ray nanotomography (see **Supplementary Information, Section 1.3**). By accurately tracing the boundaries of the cells, the width and height of each pore were automatically calculated using ImageJ measurement tools. Then, the two-dimensional average pore size was approximated using Equation (2), where ϕ_i^x and ϕ_i^y are the i-th pore diameter in the horizontal and vertical orientations respectively.

$$\bar{\phi}_{2D} = \frac{1}{N}\sum_{i=1}^{N}\frac{\phi_i^x + \phi_i^y}{2} \tag{2}$$

Porosity

In the case of hollow fibers without superficial pores, porosity can be determined solely based on the fiber diameter (d) and wall thickness (t), assuming a constant wall thickness along the fiber, without the need for ImageJ. Porosity is quantified using a straightforward estimation shown in Equation (3), which is simply dependent on the ratio between these two magnitudes. Also, in Equation (3), V_g is the volume of gas phase contained in the fiber, and V_T is the total volume of the fiber.

$$V_f = \frac{V_g}{V_T} = \frac{\left(\frac{d}{2} - t\right)^2}{\left(\frac{d}{2}\right)^2} \tag{3}$$

The expansion ratio ER, defined as the ratio of the hollow fiber total volume (V_T) to the volume of the solid polymer (V_s) before foaming, can also be calculated using Equation (4). The expansion ratio provides insights into the extent to which volume has increased after the foaming process. It is also related to the porosity (V_f) as shown in Equation (4). See **Supplementary Information, Section 1.3** for more details.

$$ER = \frac{V_T}{V_s} = \frac{V_T}{V_T - V_g} = \frac{1}{1 - \frac{V_g}{V_T}} = \frac{1}{1 - V_f} \tag{4}$$

Surface roughness

The arithmetic average roughness (Ra) of the fibers was determined through an analysis of the 2D projections again using the "Plot profile" plugin on ImageJ. To quantify the roughness, a rectangular region of interest was defined around the fiber surface (see **Supplementary Information**, **Fig. S8**). By binarizing the image and plotting the intensity profile along the fiber surface, the peaks and valleys corresponding to surface irregularities were identified. This process was repeated for multiple projections to obtain a more representative value of *Ra* across the entire fiber surface. To convert the gray scale values of the plot profile into physical units, a change of variable was performed using the maximum to minimum peak distance. This conversion allowed for the direct measurement of surface irregularities in micrometers, providing a quantitative assessment of the imperfections present on the fiber topography (see **Figure 2**). Finally, the arithmetic average roughness, regarded as the standard deviation of the height profile along the fiber (Thomas, 1981), could be computed using Equation (5) , where $h_i(x)$ is each of the discrete points that make a discretization of the height profile $h(x)$, $\bar{h}$ is their average,

and N their total amount. Note that this method would need adjustments in images of samples with curvature.

$$Ra = \sqrt{\frac{1}{N}\sum_{i=1}^{N}\left(h_i(x) - \bar{h}\right)} \tag{5}$$

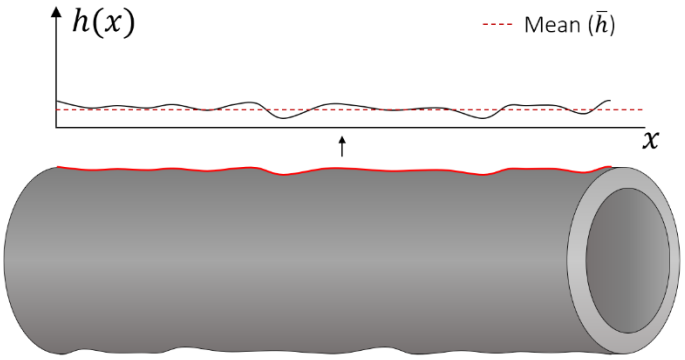

Figure 2. Schematic visualization of the calculation of the surface roughness (Ra).

3. RESULTS AND DISCUSSION

3.1 Scanning Electron Microscopy (SEM) results

The SEM images provided a first look into the morphology of the fibers. Upon examination (see **Figure 3**), the fibers displayed a consistent and homogeneous structure, reinforcing the validity of the subsequent analysis in which single fibers were taken randomly from the mat. It was also possible to observe the presence of holes and well-defined external walls in the hollow fibers, which, in some cases, show clearly inhomogeneous thickness (see **Supplementary Information, Figure S6**), as well as clearly visible surface pores exhibited in both solid and hollow fibers (see **Supplementary Information, Figure S7.a)**).

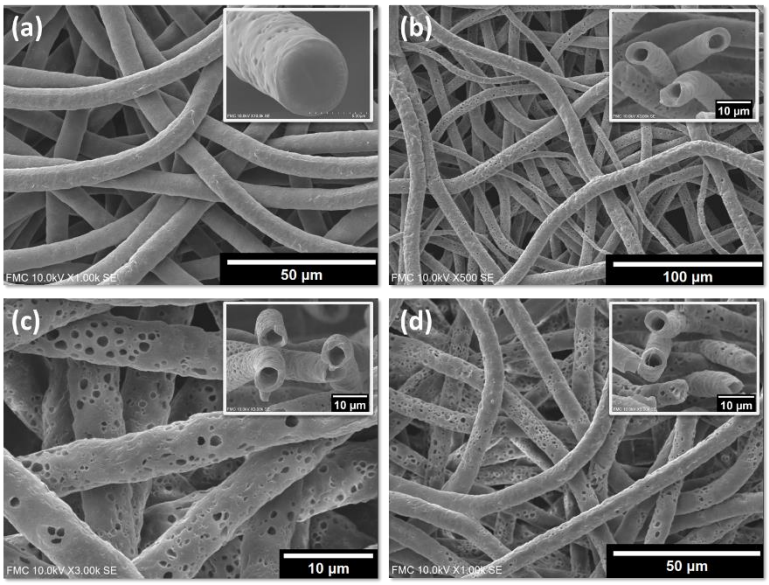

Figure 3. SEM micrographs of Fibers (a) F1, (b) F2, (c) F3, and (d) F4.

3.2 Synchrotron X-ray nanotomography results

In this section, the visual examination of the synchrotron nanotomography data is shown. **Figure 4** shows some examples of the 2D projections obtained with this experiment. These images provided a preliminary overview of the fiber shape and structure, imperfections, and internal characteristics. A cursory observation of these 2D projections also allowed for the categorization of the fiber as hollow or solid. For example, solid fibers like samples 1, 2, and 3, appear darker in the projections due to their denser and more compact structure, resulting in higher X-ray attenuation. This is visualized as a darker region in the projection images. In contrast, hollow fibers of samples 4 – 9 in **Figure 4**, which contain an internal void or cavity, exhibit lower X-ray attenuation in the inner parts as the X-rays pass through the empty space. Consequently, these hollow regions appear brighter in the 2D projections. In the cases of samples 4, 5,

7 and 8, the 2D projections provide a clear visualization of its openness, suggesting hole continuity along the fiber.

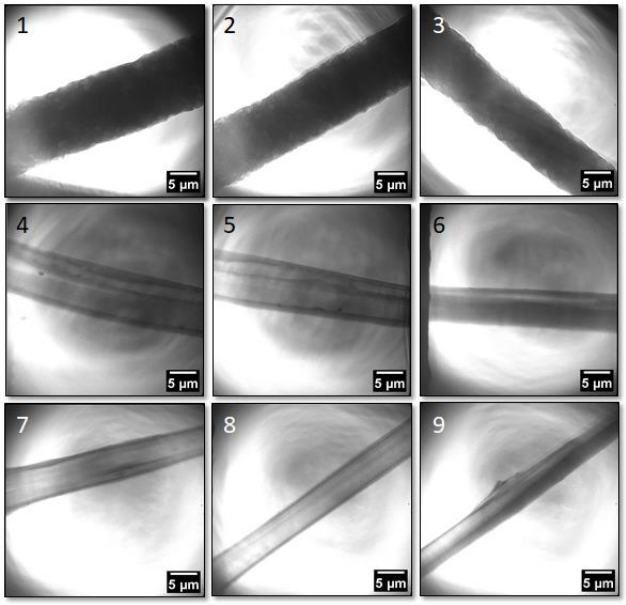

Figure 4. Representative synchrotron X-ray tomography 2D projections of the nine samples included in this study (see **Table 1**).

Figure 5 shows examples of some 3D reconstructions that could be obtained from their corresponding 2D projections. A quick overview of these reconstructions revealed insightful information about the overall morphology, allowing for a comprehensive understanding of the fibers three-dimensional shape and internal structure. Furthermore, the results showcased remarkable agreement with the 2D images in terms of morphology and the ability to detect fiber imperfections such as dust depositions or shape irregularities. This is even in spite of the original images not covering the whole range of 360º (see **Supplementary Information, Table S1**). However, it is important to note the limitations encountered during the analysis. In some cases, the fiber closure was not well-defined, which could be attributed to this limited number of projections used in the reconstruction process. Additionally, the fibers appeared slightly flattened in the

reconstructions, possibly indicating deformation or damage incurred during handling, despite their circular appearance in the SEM images. This flattening effect was also observed in the 2D projections, further supporting the presence of fiber deformation. In this case, the 3D reconstructions provided clear confirmation of the continuity and openness of the hollow structure along the entire length of the fiber segments, further validating the results obtained from the 2D projections. While the 2D projections alone can provide some assessment of hole continuity, the 3D reconstructions offered a more comprehensive and unambiguous visualization, leaving no doubt about the reliability of the results.

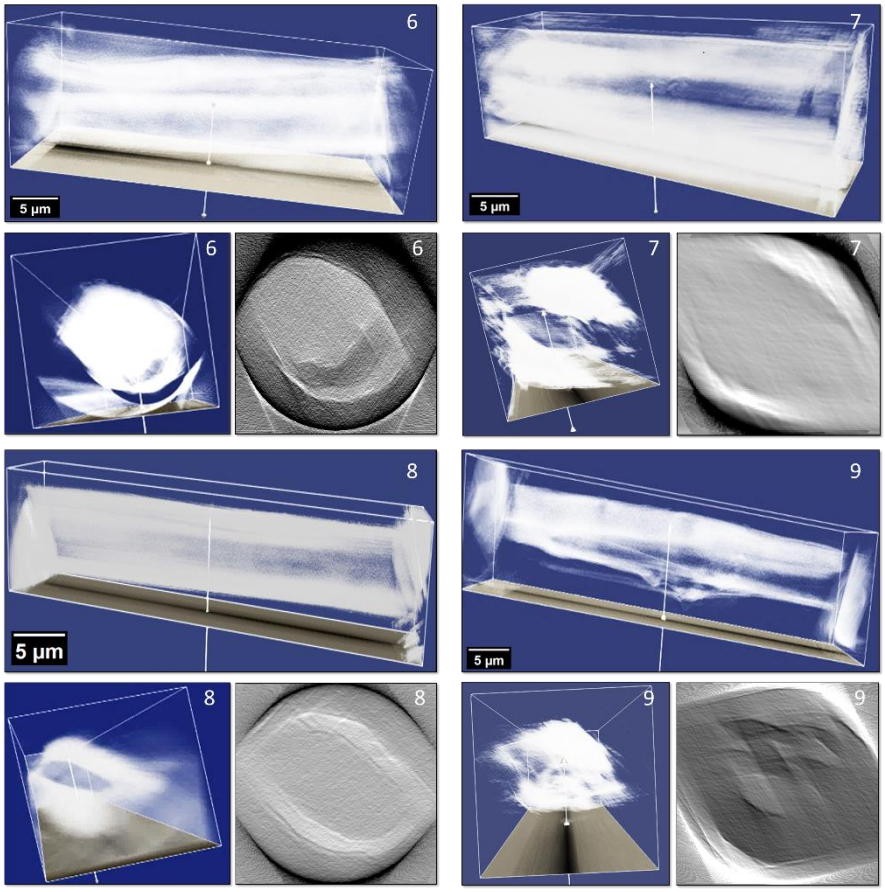

Figure 5. Representative examples of 3D reconstructions. Samples 6 - 9. For each sample, the longitudinal view, together with two cross-sectional views (one from Tomviz (right) and one from ImageJ (left)) are shown.

These visual results provide a clear visualization of the fiber overall properties, guiding further analysis and quantification of the parameters that characterize the fiber structure and morphology. A complete and thorough analysis must be carried out by combining the insights obtained from both 2D radiographies and 3D reconstructions.

3.3 Determination of fiber parameters

Wall thickness

The characterization of fiber wall thickness was successfully achieved with both aforementioned approaches. A schematic overview of the results of every possible case can be found in **Figure 6**. Two results of the thickness are given for the 3D case as it can be computed in two opposite walls. However, in the 2D projections case, as every projection corresponds to a different tilt angle, the average of both values is given. The obtained values of wall thickness are exposed in **Table 2**. The results obtained exhibited remarkable similarity in both characterization methods, reaffirming their reliability and consistency. The value of 6.46 μm observed in sample 6 stands in glaring contrast to the other measured values of wall thickness due to the fact that the hole within the fiber is positioned far from the center and thinner than those of other samples, resulting in an uneven distribution of wall thickness. As a consequence, one side of the fiber exhibits a considerably higher wall thickness compared to the rest (refer to **Figure 4**).

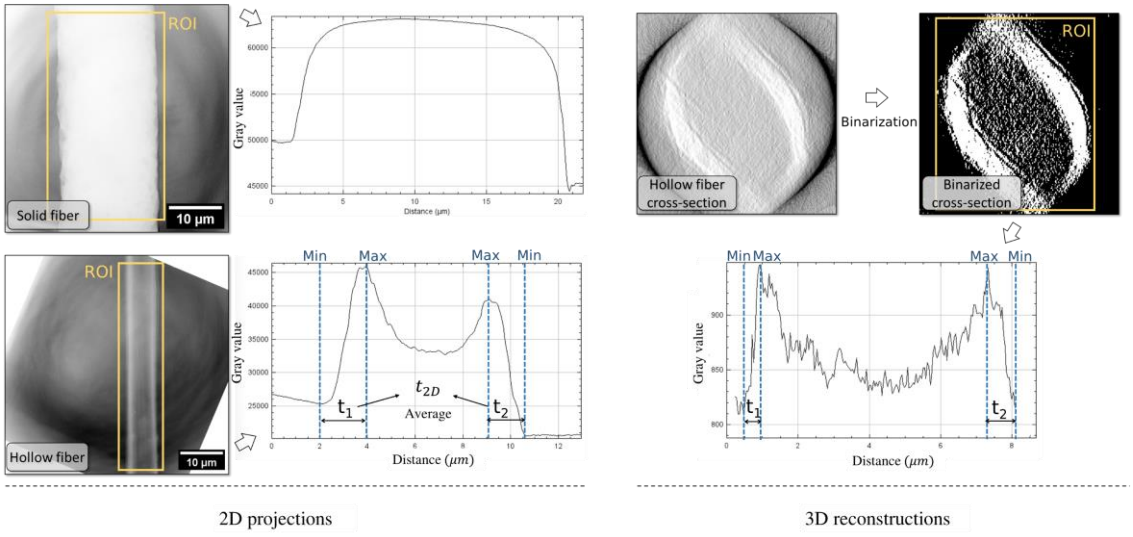

Figure 6. Examples of intensity profiles for the three cases: solid fiber and hollow fiber from 2D projections, and hollow fiber cross-section from 3D reconstruction.

Table 2. Results of wall thickness from both 2D projections and 3D reconstructions for the larger and shorter walls of every sample.

Sample	t_{3D} (μm)		t_{2D} (μm)
	t_1	t_2	
4	2.12 ± 0.23	1.76 ± 0.35	2.49 ± 0.61
5	1.60 ± 0.20	0.95 ± 0.24	1.32 ± 0.15
6	6.46 ± 0.96	1.05 ± 0.16	3.71 ± 0.30
7	1.70 ± 0.28	1.17 ± 0.16	1.54 ± 0.47
8	1.25 ± 0.27	1.08 ± 0.15	1.45 ± 0.20
9	2.71 ± 0.36	1.51 ± 0.41	2.68 ± 0.61

Upon closer examination, it was observed that the ratio of thicknesses t_{3D}/t_{2D} was slightly lower than one in general (see **Figure 7**), with the only exception being sample 6, for the reasons explained before. This means that the 3D reconstructions-based approach yielded slightly lower wall thickness values compared to the 2D projections, which indicates that the 3D reconstructions provide a more conservative estimation of the wall thickness. Several factors could contribute to this observed difference. One possibility is the reconstruction process, which may introduce some level of distortion or

loss of information. Additionally, the binarization process in ImageJ, which plays a crucial role in segmenting the fiber from the background, may have involved the deletion of a small, but appreciable number of external pixels with values close to the ones in the background. However, the deviations from the ideal value are not significantly large, which proves a certain agreement between the two characterization methods.

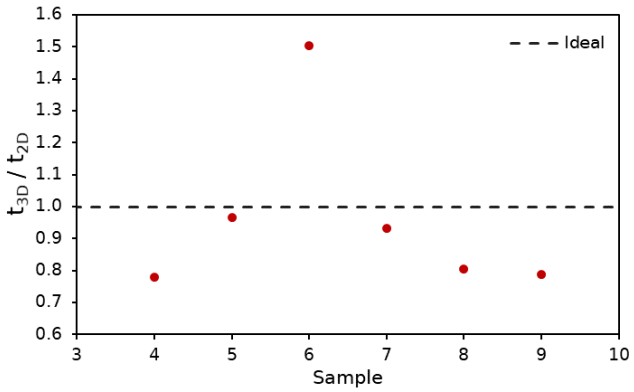

Figure 7. Wall thickness ratios of both techniques. In the case of t_{3D}, the thickness of both sides was averaged.

Wall thickness distribution

The wall thickness distribution was successfully quantified, this time, using the 2D radiography projections. 3D reconstructions were not used in this case given that, although it is achievable, the values of wall thickness can be subjected to image processing bias, as exposed in the previous subsection. Two examples of wall thickness distributions can be seen in **Figure 8**. In the case of sample 8, the uniformity in the measured wall thickness across different sections of the fiber suggests that the hollow structure maintains its integrity and extends throughout the entire length of the segment. In sample 9, even though the hollow structure does not have a central symmetry, the wall thickness never tends towards the diameter of the fiber, also indicating hole continuity.

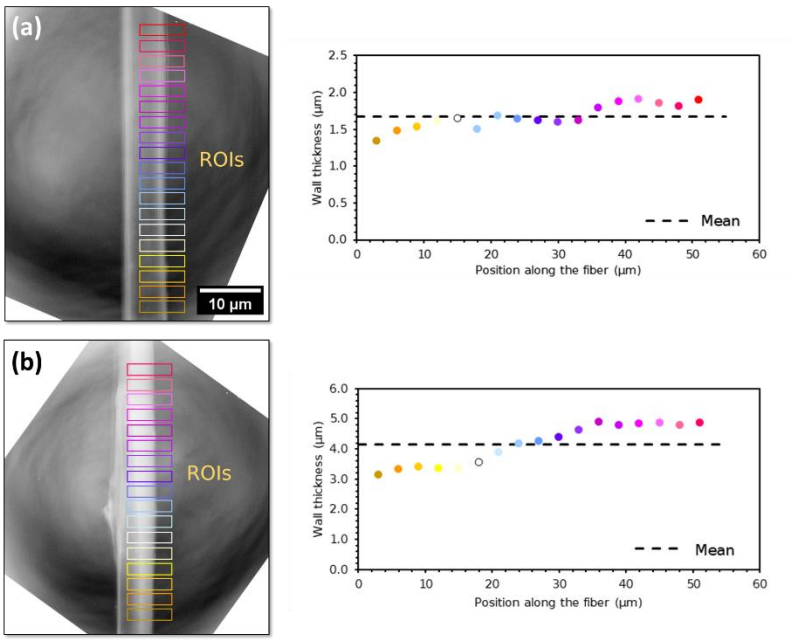

Figure 8. Example of ROIs and wall thickness distribution corresponding to samples (a) 8 and (b) 9.

The histograms in **Figure 9**illustrate the frequency distribution of the wall thickness values of fibers F2, F3 and F4. Fiber F2 exhibits a normal-like distribution in its histogram. The majority of the wall thickness values fall within the range of 2.0 - 2.5 μm, indicating a relatively consistent thickness for this fiber, with some minor variations observed. In the case of fiber F3, the histogram shows a bimodal shape. This shows that fiber F3 possesses a non-uniform wall thickness around its shape, with the hole being displaced from the center, resulting in different wall thicknesses on opposite sides of the fiber. This could also be qualitatively seen in the **Supplementary Information, Figure S6**, or in **Figure 4**, sample 6. Lastly, for fiber F4, it can be observed that the majority of segments exhibited a relatively consistent wall thickness, with a narrow range of values between 1.0 and 2.0. However, some segments displayed variations in the wall thickness, indicating potential structural heterogeneity. The histograms corresponding to F2 and F4

contain the data from at least two samples of each fiber, which contributes to assess the continuity of the inner hole in a more representative manner, overcoming the limitations caused by the low field of vision.

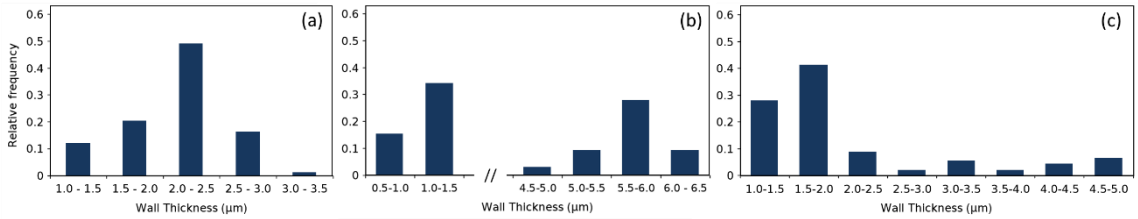

Figure 9. Wall thickness relative frequency histograms corresponding to fibers (a) F2, (b) F3, and (c) F4.

Overall, the successful determination of the wall thickness distribution using the 2D projections highlights the capability of this technique to provide valuable information about the morphological characteristics of the fibers.

Pore size

The pore size calculation of fiber F1 obtained from images such as the example projection displayed in **Figure 10.a)** yielded the frequency histogram shown in **Figure 10.b)**. The histogram exhibits a bell-shaped distribution, resembling a normal distribution curve. The peak was observed in the range of 0.3 to 0.4 μm, indicating a prevalent pore size within this interval, which is influenced by the electrospinning process and can have implications for various applications requiring controlled pore characteristics. The value is also in correspondence with the average pore size value. The normal distribution shape implies a balanced distribution of smaller and larger pores. These results are found to be in agreement with the pore size values obtainable using SEM micrographs (**Supplementary Information, Figure S7.a)**) whose mean value falls within 0.3 –

0.4 μm. In this case, both methods would provide consistent measurements, although SEM exhibits a clearer visibility for this purpose.

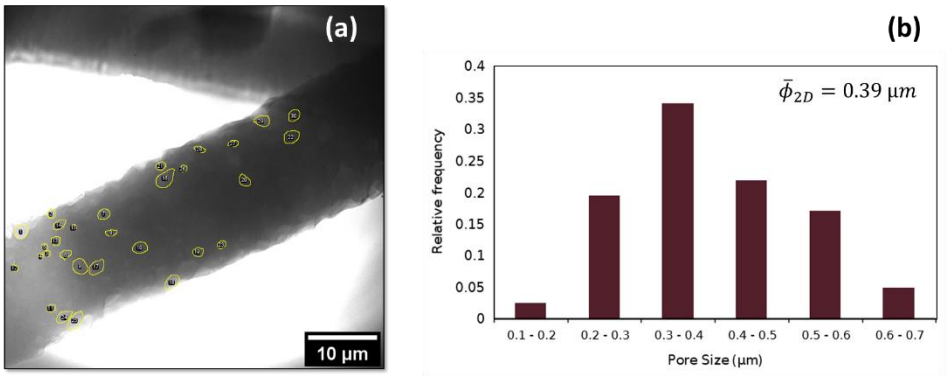

Figure 10. (a) Identification of individual pores. (b) Pore size frequency histogram and two-dimensional mean pore size of fiber F1.

The pore size calculation was not possible to perform in any sample that underwent the gas dissolution process. This is due to the complete lack of visible pores in the 2D projections, regardless of the known presence of pores as evidenced by SEM (see **Figure 3**). A possible explanation for the increased visibility of pores in solid fibers compared to hollow fibers in X-ray nanotomography is related to the contrast mechanism employed in the imaging technique. X-ray tomography relies on the attenuation of X-rays as they pass through the sample. In solid fibers, the presence of pores creates localized regions with lower X-ray attenuation due to the large difference in density between the solid fiber and the void spaces of the surface pores. This density contrast leads to a higher contrast between the pore regions and the surrounding solid material, making the pores more distinguishable in the resulting images. On the other hand, in hollow fibers, the absence of a solid material within the central region reduces the density contrast provided by the polymer, making the pores less visible in the tomographic reconstructions (i.e., the contrast between the void surface pores and the mostly empty fibers is not enough to

detect the surface pores, which can be overlapped by the noticeable variations of the flatfield).

Porosity

The results of porosity and expansion ratio obtained by wall thickness and fiber diameter measurements derived from the 2D projections are shown in **Table 3**. It is important to clarify again that this method (Equation (3)), neglects superficial pores. The values indicate significant variations among the different samples. Sample 6 exhibits the lowest porosity, and thus, expansion ratio, indicating a relatively compact and solid structure with low pore presence, which can be directly seen from its corresponding images in **Figure 4** and **Figure 5**. Samples 4, 5, 7 and 8, on the other hand, show relatively high porosities and expansion ratios, which demonstrates the successful fabrication of hollow structures with high porosity using gas dissolution foaming. The obtained values suggest that these hollow fibers could offer a substantially higher surface area in comparison with solid fibers for its use in potential applications such as filtration or controlled drug release systems. Those values are also in good agreement with the qualitative examination that can be carried out simply looking at the images in **Figure 4** and **Figure 5**.

Table 3. Results of porosity for samples 4 – 9 in **Table 1.** Fibers used in the study.

Sample	**4**	**5**	**6**	**7**	**8**	**9**
Porosity	0.35	0.62	0.04	0.47	0.44	0.12
ER	1.55	2.62	1.05	1.87	1.79	1.14

Surface roughness

The surface roughness analysis of the fibers was carried out using the 2D projections technique. The computation of surface roughness was limited to solid fibers due to several

reasons. Firstly, similar to the challenge faced in calculating pore size, the low contrast within hollow fibers made it difficult to accurately assess the surface roughness. The absence of visible pores in the surface resulted in a lack of distinct features that could be used to quantify roughness effectively. Secondly, despite a pixel size of $20\ nm$, the low definition of the hollow fiber edges posed a significant obstacle in accurately measuring the roughness of hollow fibers. Surface roughness analysis demands precise identification of boundaries and surface irregularities, which becomes more challenging when dealing with faint or indistinct edges. The less well-defined edges of the hollow fibers hindered the visual precision required for accurate roughness calculations. Lastly, the presence of a non-flat and challenging background further complicated the computation of surface roughness in hollow fibers. Sometimes, the inadequate separation between fiber and background in terms of visual contrast made it arduous to differentiate and isolate the fiber surface.

The results of the arithmetic average roughness (Ra) for samples 1-3 are shown in **Figure 11**. They reveal variations across different samples, indicating the presence of diverse surface textures. The plot presented in **Figure 11** illustrates three examples of surface height distribution of single projections of samples 1-3, providing a quantitative representation of the surface irregularities. Each example represents a single projection; however, it is important to note that the arithmetic average roughness (Ra) values presented in the figure were obtained using an analysis conducted across multiple projections. Approximately 30 projections were utilized in each example to calculate the Ra value, ensuring a more representative and accurate estimation. The results show accurate correspondence with the real 2D projections, which demonstrates the

effectiveness of the technique in capturing and quantifying the surface roughness of electrospun fibers.

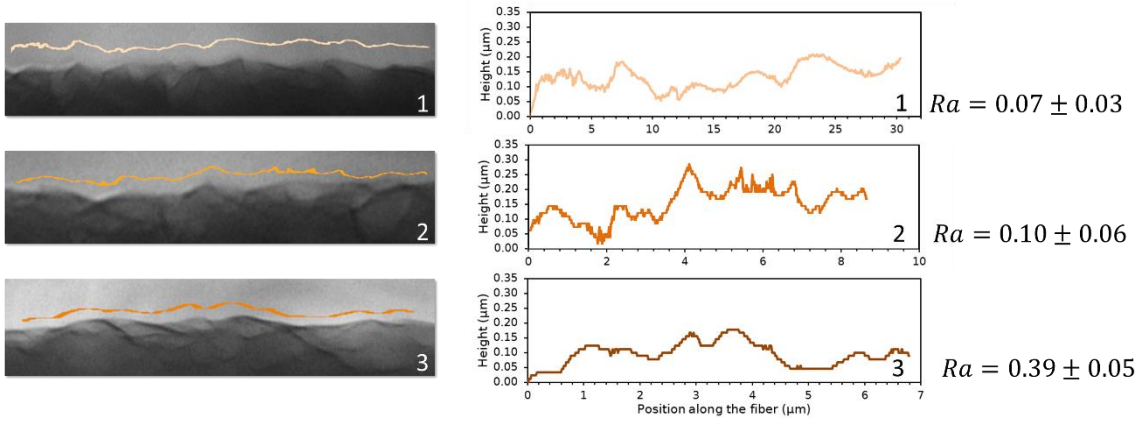

Figure 11. Examples of height distribution for samples 1, 2 and 3, and results of the arithmetic average roughness for those samples.

4. CONCLUSIONS

This study introduces a new method for the characterization of hollow polymeric fibers morphology and structure using synchrotron X-ray nanotomography together with ImageJ post-image analysis. Two approaches for data treatment were utilized: a 3D reconstruction-based analysis and a 2D projections-based analysis. This combined approach allowed for a thorough investigation of the electrospun fibers morphology and structure, given that both methods cover each other capability gaps.

The technique not only allows to obtain valuable qualitative insights into the overall fiber structure, but also quantitative information about the parameters that fully characterize the morphology. Parameters such as diameter, wall thickness, pore size, porosity and surface roughness were successfully determined for fibers with diameters of

a few microns. It is worth noting that this technique offers unique capabilities not achievable by other means, such as the ability to assess hole continuity and obtain a wall thickness distribution. The 3D reconstruction-based analysis provided a rigorous and detailed visualization of the samples external and internal structure not achievable only by analyzing the 2D projections, at the same time as ImageJ facilitated quantitative measurements on the reconstructed 3D image. The method complemented the 2D projections with the assessment of the continuity of the fibers hollowness. On the other hand, the 2D projections-based approach provided a simpler but rather precise way of calculating some fiber parameters that could not be obtained from the 3D reconstruction for diverse reasons such as the lack of useful tomography data, low contrast, or low reconstructed fiber sharpness.

All in all, this method offers a powerful tool for in-depth understanding and analysis of fiber properties, enabling advancements in various applications requiring precise control over fiber morphology and structure. The authors thank the Helmholtz-Zentrum Berlin für Materialien und Energie for the allocated beam time at BESSY II.

5. ACKNOWLEDGMENTS

Financial assistance from MCIN/AEI/10.13039/501100011033 and the EU NextGenerationEU/PRTR program (PLEC2021-007705), Regional Government of Castilla y León and the EU-FEDER program (CLU-2019-04 and VA202P20), and Ministerio de Ciencia e Innovación, EU NextGenerationEU/ PRTR program, Regional Government of Castilla y León, and EU-FEDER program “Plan Tractor En Materiales Avanzados Enfocado A Los Sectores Industriales Claves En Castilla Y León:

Agroalimentario, Transporte, Energía Y Construcción (MA2TEC)" are gratefully acknowledged.

6. REFERENCES

ABRÀMOFF, M. D., MAGALHÃES, P. J. & RAM, S. J. (2004). Image processing with imageJ. *Biophotonics International* **11**, 36–41.

ANGEL, N., GUO, L., YAN, F., WANG, H. & KONG, L. (2020). Effect of processing parameters on the electrospinning of cellulose acetate studied by response surface methodology. *Journal of Agriculture and Food Research* **2**, 100015. https://doi.org/10.1016/j.jafr.2019.100015.

ARIFF, Z. M., ZAKARIA, Z., BAKAR, A. A. & NASER, M. A. M. (2016). Effectiveness of A Simple Image Enhancement Method in Characterizing Polyethylene Foam Morphology using Optical Microscopy. *Procedia Chemistry* **19**, 477–484.

BARHOUM, A. (2019). *Handbook of Nanofibers*. Springer.

BARROSO-SOLARES, S., CUADRA-RODRIGUEZ, D., RODRIGUEZ-MENDEZ, M. L., RODRIGUEZ-PEREZ, M. A. & PINTO, J. (2020). A new generation of hollow polymeric microfibers produced by gas dissolution foaming. *Journal of Materials Chemistry B* **8**, 8820–8829.

BARROSO-SOLARES, S., ZAHEDI, M. G., PINTO, J., NANNI, G., FRAGOULI, D. & ATHANASSIOU, A. (2016). Oil removal from water-oil emulsions using magnetic nanocomposite fibrous mats. *RSC Advances* **6**, 71100–71107. http://dx.doi.org/10.1039/C6RA12246A.

BARUTCU, S., ASLAN, S., KATSAGGELOS, A. K. & GÜRSOY, D. (2021). Limited-angle computed tomography with deep image and physics priors. *Scientific Reports* **11**, 1–

12. https://doi.org/10.1038/s41598-021-97226-2.

BHAT, G. (2017). *Structure and Properties of High-Performance Fibers*. Woodhead Publishing.

BLYKERS, B. K., ORGANISTA, C., BOONE, M. N., KAGIAS, M., MARONE, F., STAMPANONI, M., BULTREYS, T., CNUDDE, V. & AELTERMAN, J. (2021). Tunable X-ray dark-field imaging for sub-resolution feature size quantification in porous media. *Scientific Reports* **11**, 1–14. https://doi.org/10.1038/s41598-021-97915-y.

CASPER, C. L., STEPHENS, J. S., TASSI, N. G., CHASE, D. B. & RABOLT, J. F. (2004). Controlling surface morphology of electrospun polystyrene fibers: Effect of humidity and molecular weight in the electrospinning process. *Macromolecules* **37**, 573–578.

CHEN, Y., STELMACOVICH, G., MULARCZYK, A., PARKINSON, D., BABU, S. K., FORNER-CUENCA, A., PYLYPENKO, S. & ZENYUK, I. V. (2023). A Viewpoint on X-ray Tomography Imaging in Electrocatalysis. *ACS Catalysis* 10010–10025.

CIMAVILLA-ROMÁN, P., PÉREZ-TAMARIT, S., BARROSO-SOLARES, S., PINTO, J. & RODRÍGUEZ-PÉREZ, M. Á. (2022). Sub-pixel Tomographic Methods for Characterizing the Solid Architecture of Foams. *Microscopy and Microanalysis* **28**, 689–700.

CUADRA-RODRÍGUEZ, D., BARROSO-SOLARES, S., RODRÍGUEZ-PÉREZ, M. A. & PINTO, J. (2022). Production of cellular polymers without solid outer skins by gas dissolution foaming: A long-sought step towards new applications. *Materials and Design* **217**.

DAS, S., PASHMINEHAZAR, R., SHARMA, S., WEBER, S. & SHEPPARD, T. L. (2022). New Dimensions in Catalysis Research with Hard X-Ray Tomography. *Chemie-Ingenieur-Technik* **94**, 1591–1610.

DeFrates, K. G., Moore, R., Borgesi, J., Lin, G., Mulderig, T., Beachley, V. & Hu, X. (2018). Protein-based fiber materials in medicine: A review. *Nanomaterials* **8**.

Doan, T. Q., Leslie, L. S., Kim, S. Y., Bhargava, R., White, S. R. & Sottos, N. R. (2016). Characterization of core-shell microstructure and self-healing performance of electrospun fiber coatings. *Polymer* **107**, 263–272. http://dx.doi.org/10.1016/j.polymer.2016.10.062.

Duan, X., Chen, H. lan & Guo, C. (2022). Polymeric Nanofibers for Drug Delivery Applications: A Recent Review. *Journal of Materials Science: Materials in Medicine* **33**.

Elahi, M. F. & Lu, W. (2013). Core-shell Fibers for Biomedical Applications-A Review. *Journal of Bioengineering & Biomedical Science* **03**, 1–14.

Ferreira, P., Alves, P., Coimbra, P. & Gil, M. H. (2015). Improving polymeric surfaces for biomedical applications: a review. *Journal of Coatings Technology and Research* **12**, 463–475. http://dx.doi.org/10.1007/s11998-015-9658-3.

Guttmann, P., Werner, S., Siewert, F., Sokolov, A., Schmidt, J.-S., Mast, M., Brzhezinskaya, M., Jung, C., Follath, R. & Schneider, G. (2018). The New HZB X-Ray Microscopy Beamline U41-PGM1-XM at BESSY II. *Microscopy and Microanalysis* **24**, 206–207.

Halicka, K. & Cabaj, J. (2021). Electrospun nanofibers for sensing and biosensing applications—a review. *International Journal of Molecular Sciences* **22**, 1–24.

Han, D. & Steckl, A. J. (2019). Coaxial Electrospinning Formation of Complex Polymer Fibers and their Applications. *ChemPlusChem* **84**, 1453–1497.

He, C. L., Huang, Z. M., Han, X. J., Liu, L., Zhang, H. S. & Chen, L. S. (2006). Coaxial electrospun poly(L-lactic acid) ultrafine fibers for sustained drug delivery. *Journal*

of Macromolecular Science, Part B: Physics **45 B**, 515–524.

JI, Y., LI, B., GE, S., SOKOLOV, J. C. & RAFAILOVICH, M. H. (2006). Structure and nanomechanical characterization of electrospun PS/clay nanocomposite fibers. *Langmuir* **22**, 1321–1328.

KUMAR, V. & SUH, N. P. (1988). 'Process Synthesis for Manufacturing Microcellular Thermoplastic Parts: a Case Study in Axiomatic Design.' Massachusetts Institute of Technology http://hdl.handle.net/1721.1/14616.

LANG, J. T., KULKARNI, D., FOSTER, C. W., HUANG, Y., SEPE, M. A., SHIMPALEE, S., PARKINSON, D. Y. & ZENYUK, I. V. (2023). X-ray Tomography Applied to Electrochemical Devices and Electrocatalysis. *Chemical reviews* **123**, 9880–9914.

LI, Y. & WAN, W. (2017). Exploring Polymer Nanofiber Mechanics: A review of the methods for determining their properties. *IEEE Nanotechnology Magazine* **11**, 16–28.

LIU, LAIJUN, ZHANG, T., LI, C., JIANG, G., WANG, F. & WANG, L. (2021). Regulating surface roughness of electrospun poly(ε-caprolactone)/β-tricalcium phosphate fibers for enhancing bone tissue regeneration. *European Polymer Journal* **143**, 110201. https://doi.org/10.1016/j.eurpolymj.2020.110201.

LIU, XIAOYANG, RONNE, A., YU, L. C., LIU, Y., GE, M., LIN, C. H., LAYNE, B., HALSTENBERG, P., MALTSEV, D. S., IVANOV, A. S., ANTONELLI, S., DAI, S., LEE, W. K., MAHURIN, S. M., FRENKEL, A. I., WISHART, J. F., XIAO, X. & CHEN-WIEGART, Y. CHEN K. (2021). Formation of three-dimensional bicontinuous structures via molten salt dealloying studied in real-time by in situ synchrotron X-ray nano-tomography. *Nature Communications* **12**. http://dx.doi.org/10.1038/s41467-021-23598-8.

LIU, XINKUAN, XU, H., ZHANG, M. & YU, D. G. (2021). Electrospun medicated nanofibers for wound healing: Review. *Membranes* **11**.

LUCY A BOSWORTH, S. D. (2011). *Electrospinning for Tissue Regeneration*. Woodhead Publishing.

MAKSIMCUKA, J., OBATA, A., SAMPSON, W. W., BLANC, R., GAO, C., WITHERS, P. J., TSIGKOU, O., KASUGA, T., LEE, P. D. & POOLOGASUNDARAMPILLAI, G. (2017). X-ray tomographic imaging of tensile deformation modes of electrospun biodegradable polyester fibers. *Frontiers in Materials* **4**, 1–11.

MITCHELL, G. R. (2011). *Electrospinning principles, practice and possibilities*. The Royal Society of Chemistry , www.rsc.org.

NYGAARD, J. V., UYAR, T., CHEN, M., CLOETENS, P., KINGSHOTT, P. & BESENBACHER, F. (2011). Characterisation of internal morphologies in electrospun fibers by X-ray tomographic microscopy. *Nanoscale* **3**, 3594–3597.

ORSI, S., DI MAIO, E., IANNACE, S. & NETTI, P. A. (2014). Hollow micro- and nano-particles by gas foaming. *Nano Research* **7**, 1018–1026.

RAMAKRISHNA, S., FUJIHARA, K., TEO, W. E., LIM, T. C. & MA, Z. (2005). *An introduction to electrospinning and nanofibers*. World Scientific.

SALEM, D. R. (2001). *Structure Formation in Polymeric Fibers*. Hanser.

SCHNEIDER, G., GUTTMANN, P., REHBEIN, S., WERNER, S. & FOLLATH, R. (2012). Cryo X-ray microscope with flat sample geometry for correlative fluorescence and nanoscale tomographic imaging. *Journal of Structural Biology* **177**, 212–223. http://dx.doi.org/10.1016/j.jsb.2011.12.023.

SENSINI, A., CRISTOFOLINI, L., FOCARETE, M. L., BELCARI, J., ZUCCHELLI, A., KAO, A. &

TOZZI, G. (2018). High-resolution x-ray tomographic morphological characterisation of electrospun nanofibrous bundles for tendon and ligament regeneration and replacement. *Journal of Microscopy* **272**, 196–206.

SHEN, H., NUTT, S. & HULL, D. (2004). Direct observation and measurement of fiber architecture in short fiber-polymer composite foam through micro-CT imaging. *Composites Science and Technology* **64**, 2113–2120.

SHKARINA, S., SHKARIN, R., WEINHARDT, V., MELNIK, E., VACUN, G., KLUGER, P., LOZA, K., EPPLE, M., IVLEV, S. I., BAUMBACH, T., SURMENEVA, M. A. & SURMENEV, R. A. (2018). 3D biodegradable scaffolds of polycaprolactone with silicate-containing hydroxyapatite microparticles for bone tissue engineering: High-resolution tomography and in vitro study. *Scientific Reports* **8**, 1–13.

SINGH, M. & SINGH, A. (2021). *Characterization of Polymers and Fibers*. Woodhead Publishing.

SOLIMAN, S., SANT, S., NICHOL, J. W., KHABIRY, M., TRAVERSA, E. & KHADEMHOSSEINI, A. (2011). Controlling the porosity of fibrous scaffolds by modulating the fiber diameter and packing density. *Journal of Biomedical Materials Research - Part A* **96 A**, 566–574.

STANGER, J., TUCKER, N. & STAIGER, M. (2005). *Electrospinning: Expert overviews covering the science and technology of rubber and plastics*. Rapra Review Reports.

THOMAS, T. R. (1981). Characterization of surface roughness. *Precision Engineering* **3**, 97–104.

TIAN, Y., WANG, Z. & WANG, L. (2021). Hollow fibers: From fabrication to applications. *Chemical Communications* **57**, 9166–9177.

Tomviz Software (n.d.). https://tomviz.org/ (Accessed May 24, 2023).

TORRE, J. (2023). ImageJ-Scripts Repository. https://github.com/Axeh99/ImageJ-Scripts.

VALENCIA-OSORIO, L. M. & ÁLVAREZ-LÁINEZ, M. L. (2021). Global View and Trends in Electrospun Nanofiber Membranes for Particulate Matter Filtration: A Review. *Macromolecular Materials and Engineering* **306**, 1–20.

VENTURA, H., SORRENTINO, L., LAGUNA-GUTIERREZ, E., RODRIGUEZ-PEREZ, M. A. & ARDANUY, M. (2018). Gas dissolution foaming as a novel approach for the production of lightweight biocomposites of PHB/natural fibre fabrics. *Polymers* **10**.

VOHRA, A., RATURI, P. & HUSSAIN, E. (2023). Scope of using hollow fibers as a medium for drug delivery. *Fiber and Textile Engineering in Drug Delivery Systems* 169–213. http://dx.doi.org/10.1016/B978-0-323-96117-2.00013-3.

WANG, J., GUO, Z. & XIONG, S. M. (2017). Characterization of the morphology of primary silicon particles using synchrotron X-ray tomography. *Materials Characterization* **123**, 354–359. http://dx.doi.org/10.1016/j.matchar.2016.12.004.

WANG, YU, PU, J., WANG, L., WANG, J., JIANG, Z., SONG, Y. F., WANG, C. C., WANG, YANFEI & JIN, C. (2016). Characterization of typical 3D pore networks of Jiulaodong formation shale using nano-transmission X-ray microscopy. *Fuel* **170**, 84–91. http://dx.doi.org/10.1016/j.fuel.2015.11.086.

WERNER, S., GUTTMANN, P., SIEWERT, F., SOKOLOV, A., MAST, M., HUANG, Q., FENG, Y., LI, T., SENF, F., FOLLATH, R., LIAO, Z., KUTUKOVA, K., ZHANG, J., FENG, X., WANG, Z. S., ZSCHECH, E. & SCHNEIDER, G. (2023). Spectromicroscopy of Nanoscale Materials in the Tender X-Ray Regime Enabled by a High Efficient Multilayer-Based Grating Monochromator. *Small Methods* **7**.

WILLIAMS, G. R., RAIMI-ABRAHAM, B. T. & LUO, C. J. (2018). *Nanofibres in Drug Delivery*. UCL Press.

WONG, S. C., BAJI, A. & LENG, S. (2008). Effect of fiber diameter on tensile properties of electrospun poly(ε-caprolactone). *Polymer* **49**, 4713–4722.

YOSHIOKA, T., DERSCH, R., TSUJI, M. & SCHAPER, A. K. (2010). Orientation analysis of individual electrospun PE nanofibers by transmission electron microscopy. *Polymer* **51**, 2383–2389. http://dx.doi.org/10.1016/j.polymer.2010.03.031.

ZOU, L., GE, M., ZHAO, C., MENG, Q., WANG, H., LIU, X., LIN, C. H., XIAO, X., LEE, W. K., SHEN, Q., CHEN, F. & CHEN-WIEGART, Y. C. K. (2020). Designing Multiscale Porous Metal by Simple Dealloying with 3D Morphological Evolution Mechanism Revealed via X-ray Nano-tomography. *ACS Applied Materials and Interfaces* **12**, 2793–2804.